OPEN ACCESS
IOP Publishing
Journal of Physics B: Atomic, Molecular and Optical Physics
J. Phys. B: At. Mol. Opt. Phys. **56** (2023) 105001 (11pp)
https://doi.org/10.1088/1361-6455/acc149

Multi-stage Stern–Gerlach experiment modeled

Lihong V Wang

Department of Electrical Engineering Andrew and Peggy Cherng Department of Medical Engineering California Institute of Technology 1200 E, California Blvd., MC 138-78, Pasadena, CA 91125, United States of America

E-mail: LVW@caltech.edu

Received 27 June 2022, revised 10 February 2023
Accepted for publication 3 March 2023
Published 25 April 2023

Abstract

In the classic multi-stage Stern–Gerlach experiment conducted by Frisch and Segrè, the Majorana (Landau–Zener) and Rabi formulae diverge far from the experimental observation while the physical mechanism for electron-spin collapse remains unidentified. Here, introducing the physical co-quantum concept provides a plausible physical mechanism and predicts the experimental observation in absolute units without fitting (i.e. no parameters adjusted), with a p-value less than one per million, which is the probability that the co-quantum theory happens to match the experimental observation purely by chance. Further, the co-quantum concept is corroborated by exactly statistically reproducing the wave function, density operator, and uncertainty relation for electron spin in Stern–Gerlach experiments.

Supplementary material for this article is available online

Keywords: Stern–Gerlach experiment, electron spin, Majorana formula, Landau–Zener formula, co-quantum dynamics

(Some figures may appear in colour only in the online journal)

1. Introduction

Performed three years before the successful development of quantum mechanics, the 1922 Stern–Gerlach experiment on silver atoms [1] quickly proved fundamental to quantum physics [2, 3]. The benchmark experiment led to the quantization of all angular momenta, discovery of electron spin, study of the measurement problem and superposition, direct investigation of the ground-state properties of atoms without electronic excitation, and selection of fully spin-polarized atoms [2]. Within a few weeks, Einstein and Ehrenfest concluded that spin collapse cannot be interpreted by radiation, which would take 100 years [4]. Recently, Wennerström and Westlund numerically simulated that relaxation of 1 μs qualitatively reproduced the double branched collapse pattern [5], and Norsen interpreted spin collapse using the de Broglie–Bohm pilot-wave theory [6]. The significance of the Stern–Gerlach experiment and relevant works are detailed in a 2016 inspiring review [2], concluding that 'The physical mechanism responsible for the alignment of the silver atoms remained and remains a mystery' and quoting Feynman, '… instead of trying to give you a theoretical explanation, we will just say that you are stuck with the result of this experiment …' [7].

Immediately, Heisenberg and Einstein proposed multi-stage Stern–Gerlach experiments to explore deeper mysteries of directional quantization [2]. Ten years later, Phipps and Stern reported the first effort [8], which was unfortunately discontinued owing to Phipps' involuntary return to the US [2]. A year later, Frisch and Segrè modified the same apparatus by adopting Einstein's suggestion on the use of

a single wire instead of three electromagnets to rotate spin; they also improved magnetic shielding, slit filtering, and signal detection [2]. Despite the use of three layers of magnetic shielding for the middle stage (i.e. the inner rotation or IR chamber), the remnant or residual fringe magnetic field was still 0.42×10^{-4} T (or 0.42 G). Rather than fight the fringe magnetic field further, they took advantage of it. The magnetic field from the wire in the middle stage cancels the remnant field to produce a magnetic null point, around which the field is approximated as a magnetic quadrupole; consequently, they successfully observed nonadiabatic spin flip [9]. Note that only the magnetic field near a null point is effective for nonadiabatic spin flip; thus, the field far from a null point does not significantly affect transition, and its detailed distribution is of little import. Frisch and Segrè varied the wire current, which is the only independent variable controlled here, over nearly two orders of magnitude approximately uniformly on a logarithmic scale to observe the peak fraction of spin flip and its entire range. They started and ended with sufficiently extreme currents that yielded negligible fractions of spin flip. Having reached a nearly zero fraction of spin flip at the highest current might be the reason that they ceased increasing the current further. Further, the calculation of the fraction automatically obviates the requirement for absolute calibration. This data set suggests they designed and executed the experiment with great care.

Frisch and Segrè found that their observation [9] unexpectedly diverges from the Majorana formula (figure 1) [10, 11], which was stimulated by the experiment of Frisch and Segrè. The Majorana formula is a variant of the Landau–Zener formula, which is better-known despite the concurrent publications of all four related papers in the same year [12–14]. For a historical comparison of the four papers, please refer to [15]. Fermi suggested that interaction among atoms could be responsible for the divergence, but atoms were sufficiently sparse to be treated independently [9]. Rabi acknowledged 'Professor E. Segrè for discussions on the details of the Frisch and Segrè experiment', recognized the role of the nuclear magnetic moment, and revised the Majorana formula through hyperfine coupling [16]. Rabi's revised formula, however, did not overcome the divergence (figure 1).

Multi-stage Stern–Gerlach (Frisch–Segrè) experiments are much more difficult to model than single-stage ones. Multiple stages produce far more nuanced observation because the middle stage can vary the electron spin orientation over a wide range after polarization by the first stage. A correct single-stage theory must pass the more stringent test of the multi-stage experiment. This spin-flip divergence in multi-stage Stern–Gerlach experiments remains unresolved [2]. One may only speculate why the 1933 discrepancy [9] has not been resolved. The seminal paper has not been republished in English, which might have limited its visibility.

Here, a theory, called co-quantum dynamics (CQD) [17], is presented to both provide a collapse mechanism and predict the Frisch–Segrè experimental observation (figure 1) [9]. CQD is theoretically verified by reproducing, for electron spin in Stern–Gerlach experiments, the quantum mechanical wave function, density operator, and uncertainty relation as well as, in a recent publication [17], the Schrödinger–Pauli equation. In section 2, CQD is presented in three subsections, including the equations of motion, branching condition, and pre-collapse state function and prediction expression. In section 3, Stern–Gerlach experiments in both single and multiple stages are modeled. For flow continuity, lengthy interpretations are postponed to section 4, and detailed mathematical derivations are presented in Appendices (supplement material). The CQD derivation of the uncertainty relation is deferred to the last appendix.

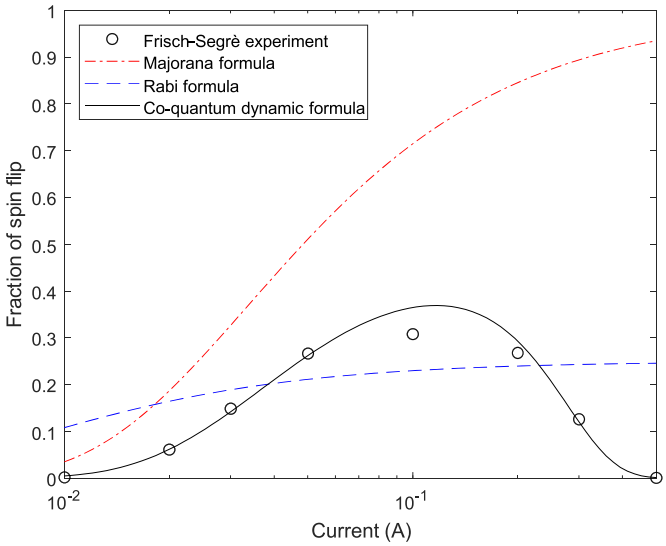

Figure 1. Illustration of the divergence of the Majorana and Rabi formulae from the Frisch–Segrè experimental observation and the convergence of the co-quantum dynamic formula. Details are to be discussed.

The following table (table 1) compares briefly CQD with the representative existing quantum mechanical theories for collapse [18], e.g. the Ghirardi–Rimini–Weber model [19] and continuous spontaneous localization model [20, 21]. CQD, based on the classical Bloch equation (or its Landau–Lifshitz–Gilbert derivative) and the two postulates, provides a physical instead of phenomenological mechanism for electron spin collapse. In the presence of an external magnetic field, the nuclear magnetic moment is responsible for the collapse of electron spin. The absence of fitting with any adjustable parameters and the high coefficient of determination R^2 (or high correlation coefficient) led to the small p-value ($p < 8 \times 10^{-7}$) [22, 23]. In general, fitting with more and more adjustable parameters, one may improve R^2 towards unity. While R^2 is not penalized for the number of adjustable parameters used relative to the number of experimental data points available, the p-value is. Therefore, one may achieve an arbitrarily high R^2 at the expense of the p-value. The p-value is an objective measure of agreement between a theory and the experiment. As a standard definition, the p-value quantifies the probability of observing results at least as extreme as the ones observed given that the null hypothesis is true. For stringent discoveries, high-energy physics,

Table 1. Comparison between representative existing quantum mechanical theories and CQD.

	Existing theories	Co-quantum dynamics
Domain	Quantum mechanical	Semiclassical
Starting equation	Schrödinger equation	Bloch equation (classical) [17]
Cause for collapse	Phenomenological: no physical object identified [18]	Physical: nuclear magnetic moment identified
Angular distribution of nuclear magnetic moment	Discrete (quantized); isotropic	Continuous; isotropic or anisotropic
Collapse rate	Preset as a constant dimensional rate ($1\ s^{-1}$)	Scaled dynamically via a dimensionless constant (equation 9)
Measurement uncertainty	Inequality	Equality (equation 186), yielding the inequality (equation 187)
Quantitative prediction of multi-stage Stern–Gerlach (Frisch–Segrè) experiment	Not found yet in the literature except the Majorana or Rabi formulae	Accurately ($p < 8 \times 10^{-7}$) without scaling or fitting, no parameters are adjusted

for example, requires $p \leqslant 3 \times 10^{-7}$, which corresponds to 5σ [24]. The Laser Interferometer Gravitational-wave Observatory (LIGO) observation of gravitational waves applied a similar criterion [25]. The agreement of CQD with the experiment is at a similar level as well. While the LIGO observed a chirp signal, which is common in various forms in nature, the Frisch–Segrè experimental data follow an uncommon shape, which is even more unlikely to be matched by random chance. Therefore, the value of $p < 8 \times 10^{-7}$ claims a statistical significance that cannot be ignored objectively. The probability that CQD happens to match the experimental observation so well purely by chance is less than one in a million. It is even less likely for an incorrect theory to match an incorrect experiment by chance if one doubts the Frisch–Segrè experimental data. Because the Majorana or Rabi formula, if correct, follows a monotonic trend, it would be difficult to fathom that some experimental imperfections caused the fraction of spin flip to increase at low currents and to decrease at high currents. Matching a theory with the experiment so well without using any adjustable parameters inspires conviction. Further, CQD is corroborated by statistically reproducing exactly the wave function, density operator, and uncertainty relation for electron spin. This corroboration may be considered supporting evidence because an incorrect theory would highly unlikely be able to reproduce so many fundamental aspects of quantum mechanics.

2. Methods

2.1. CQD equations of motion

In classical electrodynamics, the motion of a magnetic dipole moment, $\vec{\mu}$, is described by the Bloch equation,

$$\frac{\mathrm{d}\hat{\mu}}{\mathrm{d}t} = \gamma\hat{\mu} \times \vec{B}, \tag{1}$$

where caret denotes a unit vector, t time, γ the gyromagnetic ratio, and $\vec{B}$ the magnetic flux density. Majorana stated that both the classical and the quantum-mechanical treatments on spin flip require integration of the same differential equations [10, 11]. It is known that the Schrödinger or von Neumann equation for a unitary two-level system can be converted to the Bloch equation or its analog [7, 26, 27].

We now extend the Bloch equation to the Landau–Lifshitz–Gilbert equation [28],

$$\frac{\mathrm{d}\hat{\mu}}{\mathrm{d}t} = \gamma\hat{\mu} \times \vec{B} - k_i\hat{\mu} \times \frac{\mathrm{d}\hat{\mu}}{\mathrm{d}t}, \tag{2}$$

where the dimensionless k_i is called the induction factor here. Although this equation was originally intended for condensed matter, the underlying physical mechanism for the added term is compatible with CQD (see paragraph 1 in section 4). In fact, the author had developed CQD before realizing its connection with the Landau–Lifshitz–Gilbert equation. If $k_i = 0$, the Bloch equation is recovered.

Henceforth, subscripted e and n denote electron and nucleus, respectively. The default atom, to match the Frisch–Segrè experiment [9], is potassium (^{39}K). The scope of the manuscript is limited to potassium in the Stern–Gerlach or Frisch–Segrè experiment.

The torque-averaged magnetic flux densities from $\vec{\mu}_n$ and $\vec{\mu}_e$ applied on each other are respectively (appendix 1)

$$\vec{B}_n = \frac{5\mu_0}{16\pi R^3}\vec{\mu}_n \tag{3}$$

and

$$\vec{B}_e = \frac{5\mu_0}{16\pi R^3}\vec{\mu}_e, \tag{4}$$

where μ_0 is the vacuum permeability ($4\pi \times 10^{-7}$ H m^{-1}) and R is the van der Waals atomic radius (2.75×10^{-10} m) [29]. Chiefly because the nucleus is more massive, μ_e (9.285×10^{-24} J T^{-1}) $\gg \mu_n$ (1.977×10^{-27} J T^{-1}); thus, B_e (558.1×10^{-4} T) $\gg B_n$ (0.119×10^{-4} T), where 10^{-4} T = 1 Gauss.

CQD refers to $\vec{\mu}_e$ as the principal quantum and $\vec{\mu}_n$ in the same atom as the co-quantum. Postulate 1 states that induction between the electron and the nucleus tends to increase $|\theta_e - \theta_n|$, where θ denotes the polar angle relative to the quantization axis (see paragraph 1 in section 4). We (1) apply the Landau–Lifshitz–Gilbert equation to both $\hat{\mu}_e$ and $\hat{\mu}_n$, (2) express the unit vectors in spherical coordinates, and (3) revise

the signs of the induction terms to implement the above postulate, leading to the following CQD equations of motion (appendix 2):

$$\dot{\theta}_e = -\gamma_e \left[B_y \cos\phi_e + B_n \sin\theta_n \sin\left(\phi_n - \phi_e\right)\right] - \operatorname{sgn}\left(\theta_n - \theta_e\right) k_i \left|\dot{\phi}_e\right| \sin\theta_e, \tag{5}$$

$$\dot{\theta}_n = -\gamma_n \left[B_y \cos\phi_n + B_e \sin\theta_e \sin\left(\phi_e - \phi_n\right)\right] - \operatorname{sgn}\left(\theta_e - \theta_n\right) k_i \left|\dot{\phi}_n\right| \sin\theta_n, \tag{6}$$

$$\dot{\phi}_e = -\gamma_e \left\{B_z + B_n \cos\theta_n - \cot\theta_e \left[B_y \sin\phi_e + B_n \sin\theta_n \cos\left(\phi_n - \phi_e\right)\right]\right\} - \frac{\operatorname{sgn}\dot{\phi}_e k_i \left|\dot{\theta}_e\right|}{\sin\theta_e}, \tag{7}$$

and

$$\dot{\phi}_n = -\gamma_n \left\{B_z + B_e \cos\theta_e - \cot\theta_n \left[B_y \sin\phi_n + B_e \sin\theta_e \cos\left(\phi_e - \phi_n\right)\right]\right\} - \frac{\operatorname{sgn}\dot{\phi}_n k_i \left|\dot{\theta}_n\right|}{\sin\theta_n}. \tag{8}$$

Here, ϕ denotes the azimuthal angle; B_y and B_z represent, respectively, the y (axis of the atomic beam) and z components of the external magnetic flux densities; B_x is neglected for brevity; sgn denotes the sign function. When $\theta_e = 0$ or π, equation (7) is replaced with $\dot{\phi}_e = 0$; when $\theta_n = 0$ or π, equation (8) is replaced with $\dot{\phi}_n = 0$. Primarily because the nucleus is more massive again, γ_e (-1.761×10^{11} rad Hz T^{-1}) in absolute value is four orders of magnitude greater than γ_n (1.250×10^7 rad Hz T^{-1}). If $B_n = 0$ and $k_i = 0$, equations (5) and (7) reduce to the equations shown by Majorana [10, 11].

2.2. CQD branching condition

Postulate 2 states that the polar angle of the co-quantum, θ_n, varies negligibly ($\ll \pi$) during flight in typical Stern–Gerlach experiments, where the duration is too short for the co-quantum to collapse (see paragraph 2 in section 4). The external main field, B_0, along the z axis is usually much stronger than B_e and B_n. While the fast motion of $\hat{\mu}_e$ is precession about the main field, the secondary motion is collapse due to the induction term, which yields the following trend from equation (5):

$$\tan\frac{\theta_e(t)}{2} = \tan\frac{\theta_e(0)}{2} \exp\left[-\operatorname{sgn}\left(\theta_n - \theta_e\right) k_i \left|\Delta\phi_e(t)\right|\right]. \tag{9}$$

Here, $\Delta\phi_e$ denotes the traversed azimuthal angle (i.e. unwrapped phase). If the Larmor frequency of the electron magnetic moment ω_e is constant, we simply have $\Delta\phi_e = \omega_e t$. As time evolves, θ_e approaches either 0 or π according to the following branching condition:

$$\operatorname{sgn}\left(\theta_n - \theta_e\right) = \begin{cases} 1 & \text{if } \theta_n > \theta_e, \\ 0 & \text{if } \theta_n = \theta_e, \\ -1 & \text{else.} \end{cases} \tag{10}$$

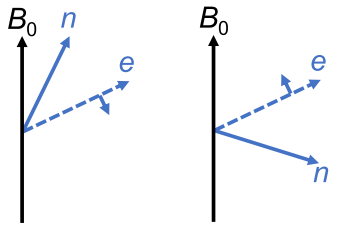

Figure 2. Examples of collapse directions determined by the branching condition in Stern–Gerlach experiments. B_0: external main field; e: electron magnetic moment (principal quantum), $\hat{\mu}_e$; n: nuclear magnetic moment (co-quantum), $\hat{\mu}_n$; short arrows: collapse directions. While $\hat{\mu}_e$ precesses about B_0 right-handedly at its Larmor frequency ($\omega_e = -\gamma_e B_0$), $\hat{\mu}_n$ does left-handedly at the Larmor frequency ($\omega_n = -\gamma_n B_0$); note that $|\omega_e/\omega_n| > 10^4$. For the same given $\hat{\mu}_e$, the collapse direction, down (left panel) or up (right panel), depends on $\hat{\mu}_n$ according to the branching condition (equation (10)). It takes on the order of N_c (estimated to be on the order of ∼220 in section 3) Larmor cycles to collapse. In typical Stern–Gerlach experiments, it is assumed that $\hat{\mu}_n$ does not collapse, i.e. θ_n is approximately constant.

Therefore, $\hat{\mu}_e$ collapses to either $+z$ or $-z$ while precessing about B_0, depending on the polar angle of the co-quantum θ_n relative to θ_e (figure 2).

The number of precession cycles required to vary $\tan(\theta_e/2)$ by a factor of e is given by

$$N_c = \frac{1}{2\pi k_i} \tag{11}$$

regardless of the strength of the external magnetic field. For a constant Larmor frequency, ω_e, the collapse time constant is

$$T_c = N_c \frac{2\pi}{|\omega_e|} = \frac{1}{k_i |\omega_e|}. \tag{12}$$

2.3. CQD pre-collapse state function and CQD prediction expression

The CQD pre-collapse state function is denoted by $|\hat{\mu}_e ©\hat{\mu}_n\rangle$, where the co-quantum, $\hat{\mu}_n$, is prefixed with © for clarity. $|\hat{\mu}_e ©\hat{\mu}_n\rangle$ represents $\hat{\mu}_e$ accompanied with $\hat{\mu}_n$, both governed by the CQD equations of motion.

The CQD prediction expression for Stern–Gerlach experiments is written as

$$|\hat{\mu}_e ©\hat{\mu}_n\rangle = C_+\left(\hat{\mu}_e, \hat{\mu}_n\right)|+z\rangle + C_-\left(\hat{\mu}_e, \hat{\mu}_n\right)\exp\left(i\phi_e\right)|-z\rangle. \tag{13}$$

The equal sign functions as a right arrow ($\rightarrow$) because the right side predicts the measurement outcome. A given $\hat{\mu}_e$ collapses to either $+\hat{z}$ or $-\hat{z}$ according to the branching condition (equation (10)). The two real and positive C coefficients take on mutually exclusive binary values while $\exp(i\phi_e)$ captures the phase information. If $\theta_n > \theta_e$, then $C_+ = 1$ and $C_- = 0$; if $\theta_n < \theta_e$, $C_+ = 0$ and $C_- = 1$. In either case, $C_+ \cdot C_- = 0$ and $C_+ + C_- = 1$.

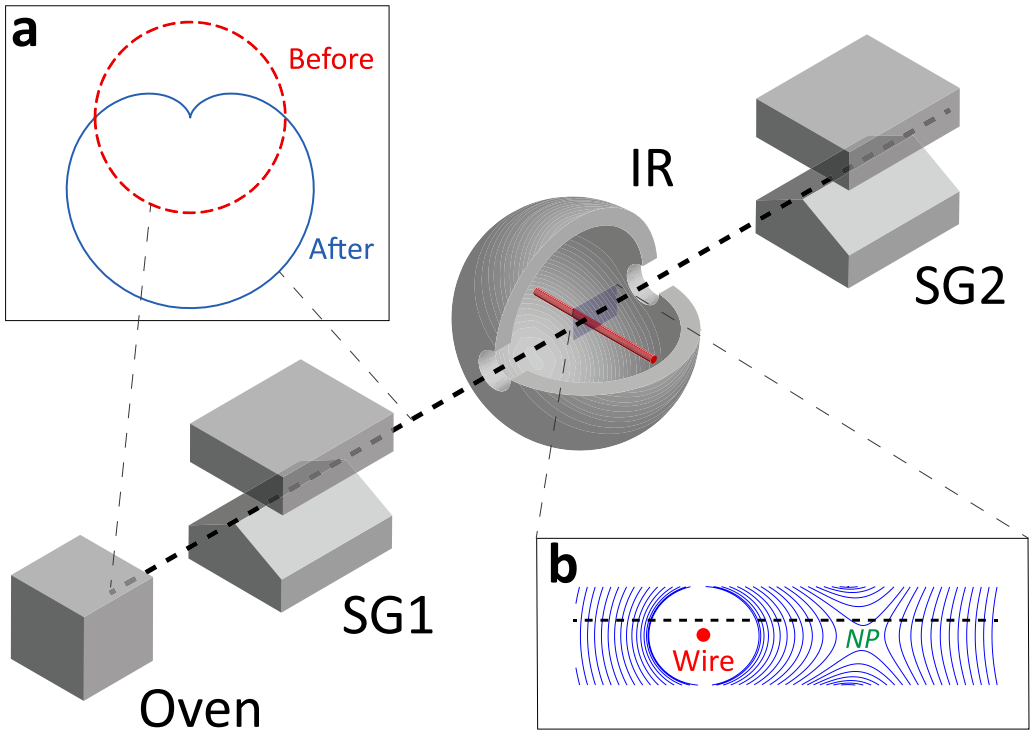

Figure 3. Multi-stage Stern–Gerlach (SG) experiment conducted by Frisch and Segrè [9]. The atomic beam from the oven is sent through (1) Stage SG1 to collapse $\hat{\mu}_e$ (principal quantum), (2) the magnetically shielded inner rotation (IR) chamber to rotate $\hat{\mu}_e$, (3) a slit (not shown) to select a branch, and (4) Stage SG2 to measure the fraction of spin flip. The red solid line and filled circle represent the current-carrying wire, and the gray sphere in cutaway view represents magnetic shielding. **Inset (a)** Angular distributions of $\hat{\mu}_n$ (co-quanta) before and after Stage SG1. **Inset (b)** Magnetic field lines within the IR chamber; NP: null point, formed by the cancelation of the magnetic field from the wire by the vertical remnant (residual) fringe magnetic field. Here, the vertical distance of the atomic beam from the center of the wire, $z_a = 1.05 \times 10^{-4}$ m; the most likely speed of atoms, $v = 800$ m s^{-1}; the uniformly distributed remnant (residual) fringe magnetic flux density, $B_r = 0.42 \times 10^{-4}$ T, which is parallel with the $+z$ axis (up in the figure); and the current carried by the wire, I, points along the $-x$ axis (into the screen).

3. Results

3.1. Single-stage Stern–Gerlach experiment

To describe the angular distribution of $\hat{\mu}_e$ or $\hat{\mu}_n$ in an ensemble of atoms, we define the angular probability density function, $p(\theta,\phi)$, as the probability of $\hat{\mu}$ pointing to the vicinity of (θ,ϕ) per unit infinitesimal solid angle, with the following normalization:

$$\int_0^{\pi}\int_0^{2\pi} p(\theta,\phi)\sin\theta \mathrm{d}\phi\,\mathrm{d}\theta = 1. \tag{14}$$

If the azimuthal distribution is isotropic, the integral reduces to $\int_0^{\pi} p(\theta,\phi)\,2\pi\sin\theta\mathrm{d}\theta = 1$.

The angular distribution of $\hat{\mu}_n$ for atoms immediately out of the oven is presumed to be isotropic as given by (figure 3, inset a, dashed circle)

$$p_{n0}(\theta_n,\phi_n) = \frac{1}{4\pi}. \tag{15}$$

In a single-stage Stern–Gerlach experiment (figure 3, SG1), the probabilities of collapse for a given θ_e are related to the binary coefficients through ensemble averaging of the pre-averaging density operator defined in appendix 3 (equation (70)) over p_{n0}. The outcome is summarized as

$$\langle C_+\rangle_n^2 = \int_{\theta_e}^{\pi} p_{n0}2\pi\sin\theta_n\mathrm{d}\theta_n = \cos^2\frac{\theta_e}{2} \tag{16}$$

and

$$\langle C_-\rangle_n^2 = \int_0^{\theta_e} p_{n0}2\pi\sin\theta_n\mathrm{d}\theta_n = \sin^2\frac{\theta_e}{2}. \tag{17}$$

The angle brackets, with the subscripts denoting nuclear, represent ensemble averaging with the integration limits determined by the branching condition (equation (10)). The two probabilities are proportional to the solid angles formed by the down and up sides of the cone shaped by the initial Bloch vector [15] precessing over one cycle. Each solid angle determines the probability of having the co-quantum on the corresponding side of the cone.

From equations (16) and (17), the pre-collapse state function (equation (13)) averages to the following familiar

quantum mechanical wave function for a pure state (appendix 3):

$$|\hat{\mu}_e\rangle = \cos\frac{\theta_e}{2}|+z\rangle + \sin\frac{\theta_e}{2}\exp(i\phi_e)|-z\rangle. \tag{18}$$

If $\hat{\mu}_e$ is also isotropically distributed as

$$p_{e0}(\theta_e,\phi_e) = \frac{1}{4\pi}, \tag{19}$$

the probabilities of collapse are predicted by averaging equations (16) and (17) over p_{e0} (appendix 3):

$$\langle C_+\rangle^2_{n,e} = \int_0^\pi \cos^2\frac{\theta_e}{2} p_{e0} 2\pi \sin\theta_e \mathrm{d}\theta_e = \frac{1}{2} \tag{20}$$

and

$$\langle C_-\rangle^2_{n,e} = \int_0^\pi \sin^2\frac{\theta_e}{2} p_{e0} 2\pi \sin\theta_e \mathrm{d}\theta_e = \frac{1}{2}. \tag{21}$$

The e subscripts denote electron. The outcomes agree with the familiar quantum mechanical prediction for a maximally mixed state of atoms immediately out of the oven, represented by a density operator (equation (87), appendix 3).

3.2. *Multi-stage Stern–Gerlach experiment*

In the multi-stage Stern–Gerlach experiment conducted by Frisch and Segrè (figure 3) [9], Stage SG1 collapses $\hat{\mu}_e$ into two branches. The inner rotation (IR) chamber rotates $\hat{\mu}_e$ by an angle of α_r using the magnetic field shown in inset b. A slit (not shown) selects one branch: the $+z$ branch is chosen here. Stage SG2 collapses $\hat{\mu}_e$ and measures the fraction of spin flip. Therefore, Stage SG1 serves as a polarizer, the IR chamber a rotator, and Stage SG2 an analyzer.

The probability of spin flip has been predicted [10, 11] by quantum mechanics as (see equation (17), set $\theta_e = \alpha_r$)

$$W_{\mathrm{qm}} = \langle -z|\alpha_r\rangle^2 = \sin^2\frac{\alpha_r}{2}, \tag{22}$$

which leads to the following Majorana formula (appendix 4, equation (117)) [10, 11]:

$$W_m = \exp\left(-\frac{\pi z_a}{2v}|\gamma_e|B_y\right). \tag{23}$$

Here, z_a is the vertical distance of the atomic beam from the center of the wire, and v is the most likely speed of the atoms. The spin flip is because B_z vanishes and reverses its sign near the null point (figure 3, inset b). Because B_y is inversely proportional to the current carried by the wire, I (equations (92) and (94) in appendix 4), the Majorana formula predicts a probability of spin flip approaching 100% with increasing currents (figure 4, Curve m), i.e. as $B_y \to 0$, $W_m \to 1$; yet, the experimental outcome decreases to nearly zero after peaking at 31% (figure 4, circles) [9]. Consequently, W_m yields a negative coefficient of determination (R^2). Using the dimensionless adiabaticity parameter k_m (equation (103) in appendix 4), one can express the above equation concisely as $W_m = \exp(-\pi k_m/2)$ (equation (116)). Rabi revised the Majorana formula to $W_m^{1/4}/4$ [16], which, however, overestimates the starting points, underestimates the peak, and continues to diverge thereafter; as a result, the R^2 remains negative (figure 1).

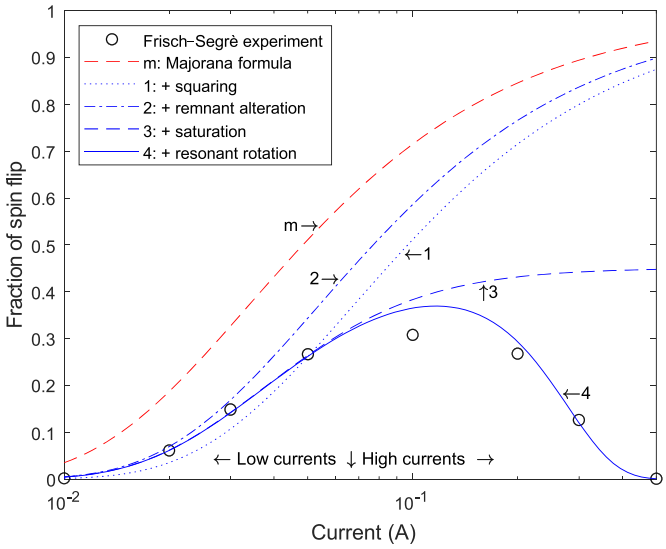

Figure 4. Fraction of spin flip versus wire current. The down arrow points to the current where $B_y' = B_n \sin\langle\theta_n\rangle$ or $k_0 = k_1$ to separate the low- and high-current regions. Curves m and 1–4 represent W_m and $W_1 - W_4$, respectively. While W_m diverges from the experiment with a negative R^2, W_3 matches the low-current experimental observation in absolute units without fitting with $R^2 = 0.9495$; further, W_4 matches the entire observation with improved $R^2 = 0.9787$ and $p < 8\times10^{-7}$. No adjustable or free parameters are used.

In CQD, Stage SG1 varies θ_n negligibly according to Postulate 2. However, polarization selection by the slit reshapes the co-quantum angular distribution from the original isotropic p_{n0} (equation (15)) to

$$p_{n1}(\theta_n,\phi_n) = p_{n0}(\theta_n,\phi_n)\cdot 2\int_0^{\theta_n} p_{e0} 2\pi\sin\theta_e \mathrm{d}\theta_e = \frac{1-\cos(\theta_n)}{4\pi}. \tag{24}$$

Here, the pre-factor 2 compensates for the overall slit rejection of the opposite polarization (equation (20)), p_{e0} is given by equation (19), and the integration limits are based on the branching condition (equation (10)). Because atoms with smaller θ_n are deflected to the blocked $-z$ branch with greater probabilities, p_{n1} forms a heart shape (figure 3, inset a, solid line; paragraph 3 in section 4).

The heart shape is assumed to be approximately maintained throughout the IR chamber owing to the extension of Postulate

2 (see paragraph 2 in section 4). The co-quanta engender the following four effects on the principal quanta.

First, the probability of spin flip is derived by ensemble averaging over p_{n1} instead of p_{n0} (equation (89) with $\theta_e = \alpha_r$ in appendix 3):

$$W_{\mathrm{cqd}} = \langle -z|\alpha_r\rangle^2 = \int_0^{\alpha_r} p_{n1} 2\pi \sin\theta_n \mathrm{d}\theta_n = \sin^4\left(\frac{\alpha_r}{2}\right), \quad (25)$$

which equals W_{qm}^2 (equation (22)). As shown by Curve 1 in figure 4, simply squaring W_m (equation (23)) already brings the solution much closer to the observation at low currents, but with an overcorrection near $I = 0.03$ A. This squaring effect evolves the probability of spin flip from W_m to

$$W_1 = W_m^2 = \exp\left(-\frac{\pi z_a}{v}|\gamma_e| B_y\right), \quad (26)$$

where B_y is computed from the remnant (residual) fringe magnetic flux density, B_r, using equations (92) and (94) in appendix 4. Using the dimensionless adiabaticity parameter k_m (equation (103)), one can express the above equation concisely as $W_1 = \exp(-\pi k_m)$ (see equation (154) in appendix 5).

Second, the z component of $\vec{B}_n$ (equation 3), represented by $B_n\cos\langle\theta_n\rangle$, offsets the upward B_r. We substitute $B_r + B_n\cos\langle\theta_n\rangle$ (equation (119) in appendix 5) for B_r to update B_y to B_y' (equation (122)). The heart shape (equation (24)) yields $\langle\theta_n\rangle = 5\pi/8$ (equation (118)). The magnitude of $B_n\cos\langle\theta_n\rangle = -0.045\times10^{-4}$ T exceeds 10% of B_r (0.42×10^{-4} T), producing an appreciable remnant-alteration effect. As shown by Curve 2 in figure 4, the corrected curve passes through the first two data circles and grazes the third one. If the co-quantum distribution were isotropic, $\langle\theta_n\rangle$ would be $\pi/2$; $B_n\cos\langle\theta_n\rangle$ would vanish, so would the remnant-alteration effect. Effect 2 evolves W_1 to (see equation (136))

$$W_2 = \exp\left(-\frac{\pi z_a}{v}|\gamma_e| B_y'\right), \quad (27)$$

where B_y', however, is computed using $B_r + B_n\cos\langle\theta_n\rangle$ instead of B_r. Using the dimensionless adiabaticity parameters k_0 (equation (125)), one can express the above equation concisely as $W_2 = \exp(-\pi k_0)$ (see equation (153)).

Third, the co-quanta saturate the rotation. As shown by equation (27), W_2 increases with decreasing B_y'. However, the weakness of B_y' is spoiled by the transverse (xy) component of $\vec{B}_n$, denoted by $B_n\sin\langle\theta_n\rangle$. Substitution of $\sqrt{B_y'^2 + (B_n\sin\langle\theta_n\rangle)^2}$ for B_y' (see equation (141)) evolves W_2 to

$$W_3 = \exp\left(-\frac{\pi z_a}{v}|\gamma_e|\sqrt{B_y'^2 + (B_n\sin\langle\theta_n\rangle)^2}\right). \quad (28)$$

Using the dimensionless adiabaticity parameters k_0 (equation (125)) and k_1 (equation (126)), one can express the above equation concisely as $W_3 = \exp\left(-\pi\sqrt{k_0^2 + k_0k_1}\right)$ (see equation (152)).

As shown by Curve 3 in figure 4, this rotation-saturation effect clamps the overshoot in Curve 2. The clamped curve passes through the first four data circles. The current is divided into two regions at 0.067 A, where $B_y' = B_n\sin\langle\theta_n\rangle = 0.11\times10^{-4}$ T. At low currents before the fourth data point ($I = 0.05$ A and $B_y' = 0.15\times10^{-4}$ T), B_y' is greater than $B_n\sin\langle\theta_n\rangle$; at high currents, conversely, $B_n\sin\langle\theta_n\rangle$ becomes dominant and saturates the curve. If the co-quantum distribution were isotropic, then $\langle\theta_n\rangle = \pi/2$; consequently, both the squaring and remnant-alteration effects (effects 1 and 2) would vanish. In this case, the rotation-saturation effect (effect 3) alone could not bring the Majorana solution down sufficiently in the low-current region because as the current decreases B_y' increasingly overpowers B_n; thus, the effect of the co-quanta would become negligible.

Combining the three effects, CQD accurately predicts the low-current observation in absolute units without fitting (i.e. no parameters are adjusted). The coefficient of determination R^2 for the low-current regime reaches 0.9495 as computed using the natural logarithm of the fractions of flip to suppress the exponential dependence (equation (28)). Therefore, effecting the three modifications to the Majorana formula has already shown evidence for the existence of both the co-quantum and the derived heart-shaped distribution.

Fourth, in the high-current regime, the precession of $\vec{B}_n$ generates substantial nuclear-resonant rotation, due to precession resonance between $\vec{\mu}_e$ and $\vec{\mu}_n$ when their Larmor frequencies are matched (see appendix 5 for details). This effect evolves W_3 to (equation (167) in appendix 5)

$$W_4 = W_3\exp\left(-c_{r1}I^3\right), \quad (29)$$

where the resonant-rotation coefficient, c_{r1}, is given by equation (163). The fraction of spin flip peaks near $I = 0.1$ A, where $B_y' = 0.074\times10^{-4}$ T, comparable to but less than $B_n\sin\langle\theta_n\rangle = 0.11\times10^{-4}$ T. As shown by Curve 4 in figure 4, this effect increases with the current and bends down Curve 3. At the maximum current ($I = 0.5$ A), $B_y' = 0.015\times10^{-4}$ T, far less than $B_n\sin\langle\theta_n\rangle$; the fraction of spin flip decreases to nearly zero. Expression of the above equation based on dimensionless parameters is discussed below equation (150). Using the dimensionless adiabaticity parameters k_0 (equation (125)) and k_1 (equation (126)) as well as f_{r1} (equation (146)), one can express the above equation concisely as $W_4 = \exp\left(-\pi\sqrt{k_0^2 + k_0k_1} - \frac{1}{2}[\pi k_1]^2 f_{r1}\right)$ (see equation (151)), where f_{r1} denotes the fraction of the Larmor period of the nuclear magnetic moment precessed during the effective flight path-length for nuclear-resonant rotation.

Combining all four effects, CQD accurately predicts the experimental observation in absolute units without fitting (figure 4, Curve 4) over the entire domain; R^2 is computed to be 0.9787 using the natural logarithm of the fractions of flip to suppress the exponential dependence (equation (29)). Under the null hypothesis that the theoretical prediction is uncorrelated with the observation, we estimate the p-value to be $< 8\times10^{-7}$ (Function *regress* or *corr*, MATLAB, MathWorks) [22, 23]. Such a small p-value further objectively confirms the existence of both the co-quantum and the derived heart-shaped

distribution. In comparison, without taking the logarithm of the fractions of flip, R^2 is computed to be 0.9621.

Thus far, we have set the induction factor $k_i = 0$ for the flight in the IR chamber, owing to the low field (appendix 5). Including k_i yields the following combined probability of spin flip (appendix 5, equation (160)):

$$W_{\mathrm{cqd}} = \exp\left[-\sqrt{(c_{r0}/I)^2 + c_{rs}^2} - c_{r1}I^3 - c_{ri}I\right], \qquad (30)$$

where c_{r0}, c_{rs}, c_{r1}, and c_{ri} represent null-point rotation, rotation saturation, nuclear-resonant rotation, and induction rotation, respectively. The current, I, controls the external magnetic field in the IR chamber. Taken from Frisch and Segrè [9], the only device-specific parameters for the predictions include B_r (0.42×10^{-4} T), z_a (1.05×10^{-4} m), and v (800 m s^{-1}). The theoretical predictions from equations (161)–(163) without adjusting any parameters are $c_{r0} = 0.054$ A, $c_{rs} = 0.80$, and $c_{r1} = 48$ A^{-3}. Substitution of these coefficients into equation (30) with $c_{ri} = 0$ produces Curve 4 in figure 4, where no free parameters are used.

Despite its small contribution in the IR chamber, the induction factor is estimated for its order of magnitude. While holding all three other parameters constant at the predicted values, fitting W_{cqd} (equation (30)) for the experimental data in figure 4 yields $c_{ri} \sim 0.57$ A. Substitution into equation (164) produces $k_i \sim 7.4 \times 10^{-4}$. Further substitution into equation (11) concludes that electron-spin collapse takes on the order of $N_c \sim 220$ precession cycles.

4. Discussion

CQD postulates that the electron and nuclear magnetic moments in an external field B_0 along z repel in the polar direction, which results in a revision to the sign of the induction term in the Landau–Lifshitz–Gilbert equation. Whereas precession is governed by the terms from the Bloch equation, collapse is modeled by the revised induction term. If $k_i = 0$, the equation of motion reduces to the Bloch or equivalent Schrödinger equation [7, 10, 11, 26, 27], which does not model collapse [30]. While precession is the dominant motion, collapse is secondary but concurrent. Although the exact mechanism for the repulsion is to be investigated, a conjecture is diamagnetism extended from orbital to spin motions. Diamagnetic magnetization, a weak but universal induction effect on all atoms, causes repulsion [31, 32]. The relativistic momentum density in the Dirac wave field shows that the magnetic moment of an electron can be attributed to a circulating flow of electric charge (equation (34) in appendix 1), similar to that in orbital motions [33]. Therefore, it is conceivable that diamagnetism applies to spin as well. In the laboratory reference frame, as $\vec{\mu}_e$ and $\vec{\mu}_n$ precess in opposite directions, each azimuthal encounter may be viewed as a 'collision', causing repulsion. Because induction is related to relative motion, the induced field on the electron may be written as $\vec{B}_i \propto \mathrm{d}\left(\hat{\mu}_e - \hat{\mu}_n\right)/\mathrm{d}t$, and the corresponding induced torque is $\vec{\tau}_i \propto \hat{\mu}_e \times \vec{B}_i$. If $\hat{\mu}_e \times \mathrm{d}\hat{\mu}_n/\mathrm{d}t$ averages out, the average induced torque becomes $\hat{\mu}_e \times \mathrm{d}\hat{\mu}_e/\mathrm{d}t$, matching the induction term in the Landau–Lifshitz–Gilbert equation. As $\hat{\mu}_e$ nears either up or down, the average induced torque approaches zero, providing stability. In the rotating reference frame that rotates at ω_e, the external B_0 vanishes, $\vec{\mu}_e$ becomes azimuthally stationary [34]; the rapidly precessing $\vec{\mu}_n$ forms in the time-average sense a cone-shaped magnet, which repels $\vec{\mu}_e$ towards $\pm z$. The sign function in the induction terms in the equations of motion is the key difference from the standard Landau–Lifshitz–Gilbert equation and is central to CQD. While standard damping always leads to a lower-energy state, collapse due to the co-quantum can reach a state of either higher or lower energy in the presence of an external magnetic field, according to the branching condition, which agrees with the Stern–Gerlach experimental observation. Numerical solutions to the CQD equations of motion, to be reported separately, have illustrated collapse with the induction term and none without. This postulate is consistent with the Pauli exclusion principle for two identical fermions, where the two magnetic moments repel towards anti-alignment. Therefore, one may regard this postulate as an extension to the Pauli exclusion principle. Note that while diamagnetism explains the collapse term, paramagnetism is expected to perturb the precession term slightly, which is neglected here.

CQD also postulates that the polar angle of $\vec{\mu}_n$ in flight varies negligibly. Because the nuclear Larmor frequency is four orders of magnitude smaller (i.e. $|\omega_n| \ll |\omega_e|$), nuclear spin collapses much more slowly than electron spin. Because no data on the collapse rates have been found in the literature, we reference the T_1 relaxation times. Typical T_1 relaxation times in electron paramagnetic resonance are on the μs scale [35], consistent with the previous estimation of the collapse time scale of $\vec{\mu}_e$ [5]. In contrast, typical T_1 relaxation times in gas-phase nuclear magnetic resonance are on the ms scale [36], indicating the order-of-magnitude collapse time of $\vec{\mu}_n$. In a typical Stern–Gerlach experiment [5, 37], the main external field B_0 along z is at least 0.3 T ($B_0 > B_e \gg B_n$, the Paschen–Back regime [16]), the length of the main field is $\sim$35 mm, and the most likely atomic speed v is $\sim$800 m s^{-1}. Consequently, the flight time through the main field is only $\sim$44 μs, which is long enough for $\vec{\mu}_e$ to collapse but too short for $\vec{\mu}_n$ to collapse. In fact, the fringe field on the source side of the main field collapses $\vec{\mu}_e$ [2]. Besides the two distinct collapse branches due to the quantization of $\vec{\mu}_e$, no additional branches due to the quantization of $\vec{\mu}_n$ have been observed by Frisch and Segrè [9] despite the prediction of up to eight branches total [38]. For $N_c \sim 220$ (equation (11)) estimated from the Frisch–Segrè experimental data shown in figure 4, the collapse time constants (T_c, equation (12) and its nuclear counterpart) at the main field strength are computed to be $\sim 3 \times 10^{-8}$ and $\sim 4 \times 10^{-4}$ s for $\vec{\mu}_e$ and $\vec{\mu}_n$, respectively, which are consistent with the above-mentioned corresponding T_1 relaxation times in orders of magnitude [35, 36]. This postulate, extended to the weaker-field IR chamber, is consistent with the selection rule for observing an electron-spin–resonance transition, stating that the magnetic quantum number of the nuclear spin remains constant (i.e. $\Delta m_I = 0$) [39].

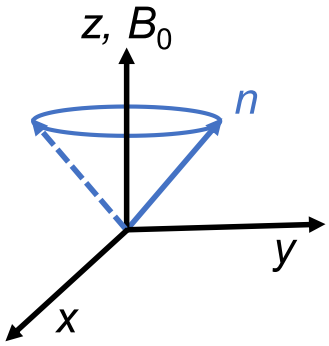

Figure 5. Illustration of the cone of $\hat{\mu}_n$ formed by precession around the external main field, B_0. n: nuclear magnetic moment (co-quantum), $\hat{\mu}_n$. Any electron magnetic moment (principal quantum), $\hat{\mu}_e$, precessing around B_0 within the cone collapses up, whereas $\hat{\mu}_e$ precessing outside the cone collapses down. For a given θ_n, the probability for the atom from the oven to reach the up branch in the single-stage Stern–Gerlach experiment is proportional to the solid angle of the cone.

The selection rule was also a major basis for Rabi's revision to the Majorana formula [16].

The heart-shaped p_{n1} in equation (24) (figure 3, inset a) can be understood in two ways. First, the integral can be perceived as the expected transmittance through Stage SG1 for a given θ_n. All principal quanta with $\theta_e < \theta_n$ collapse to $+z$, and the atoms propagate through the slit further; otherwise, the atoms are blocked by the slit. The greater the θ_n is, the greater the transmittance, proportional to the solid angle formed by the cone having a half angle of θ_n (figure 5). Second, one may examine how much principal quanta at the source around each θ_e within $\mathrm{d}\theta_e$ contribute to p_{n1}. For $\theta_e = 0$, the contribution forms a perfect spherical distribution of co-quanta because co-quanta in any direction can reach the second stage. For $0 < \theta_e < \pi$, the contribution forms a truncated sphere with the cone of $\theta_n < \theta_e$ removed because co-quanta in this range have collapsed the principal quanta to the blocked branch. For $\theta_e = \pi$, the contribution vanishes because the principal quanta are always in the blocked branch. Integrating these (truncated) spheres form the final heart shape. Conversely, the co-quantum angular distribution for the opposite branch is an inverted heart shape. Average the two complementary shapes recovers the original isotropic p_{n0}.

A key reason for the agreement between CQD and the Frisch–Segrè experimental observation is that the angular distribution of the co-quantum (i.e. the nuclear magnetic moment) is changed from an isotropic shape (equation (15)) to a continuous heart shape (equation (24)) due to the polarization. The subsequent effects are illustrated using the evolution of the curves in figure 4. As more effects are included, the model becomes more and more accurate while all parameters were given (i.e. no parameters were tuned to fit the experimental data). If the heart shape were incorrect, the agreement would be completely off. In comparison, the Majorana or Landau–Zener formula neglected the nuclear magnetic moment altogether, and Rabi used an isotropic angular distribution instead of the heart shape [16]. Note that as the wire current approaches infinity, Rabi's formula predicts a maximum of $\frac{1}{2I+1} = \frac{1}{4}$, which is well below the experimental peak of 31% (figure 1); here, $I = \frac{3}{2}$ denotes the nuclear spin number for potassium-39. Further, Rabi's standard hyperfine coupling does not contain the induction terms in CQD and hence does not model collapse. Also, the torque-averaged fields provide greater agreement than the self-averaged fields (see appendix 1).

Quantum mechanics, celebrated for its countless triumphs, still pose mysteries as discussed insightfully in recent literature [30, 40–43]. The Copenhagen interpretation construes that an electron spin is simultaneously in both eigenstates and collapses statistically upon measurement to either [7]. The collapse is not modeled by the original Schrödinger equation but stated separately as a measurement postulate [30]. Debatable inconsistency has been found in thought experiments, such as 'Schrödinger's cat' [44–46].

CQD potentially offers new insight. If co-quanta are isotropically distributed, CQD has been verified with quantum mechanics by exactly reproducing the wave function and the density operator (appendix 3) as well as the uncertainty relation (appendix 6). The probabilities of reaching the two eigenstates split according to $\cos^2\frac{\theta_e}{2} : \sin^2\frac{\theta_e}{2}$; the wave function is reproduced in equation (18). However, if the co-quanta have, for example, a heart-shaped distribution (equation (24)), the split becomes $1 - \sin^4\frac{\theta_e}{2} : \sin^4\frac{\theta_e}{2}$ (equations (88) and (89) in appendix 3); the wave function is revised accordingly (equation (90)). The density operator is found to originate from a pre-averaging counterpart with independent realizations (appendix 3). The measurement uncertainty product, explained by co-quanta, depends on the initial phase of the principal quanta and the measurement sequence, as shown by the uncertainty equality (equation (186)), which leads to the familiar quantum mechanical inequality (equation (187)). CQD has also enabled the derivation from the classical Bloch equation to the quantum Schrödinger–Pauli equation [17], while the latter has thus far been treated as a postulate.

CQD can be further tested with atoms having nuclear spins of 0 ($\mu_n = 0$), which may collapse differently in Stern–Gerlach experiments. Examples include $^{38\mathrm{m1}}$K, ^{50}K, ^{94}Ag, and ^{130}Ag, which are isotopes of the stable ^{39}K, ^{107}Ag, and ^{109}Ag. Unfortunately, these isotopes have short lifetimes ranging from 100s to 10s of ms. Note that free electrons have not been used owing to the Lorentz force and orbital magnetic moment.

Since the submission of this manuscript, our team has produced several new manuscripts to support this work. Titimbo *et al* numerically modeled the Frisch–Segrè experiment using CQD via the Bloch equation [47], whereas He *et al* numerically modeled the experiment using CQD via the Schrödinger equation [48]. Both works have numerically confirmed the analytical solution presented here and the equivalence between the Bloch equation and the Schrödinger equation stated by Majorana. Interestingly, Majorana wrote the 'Bloch' equation [10, 11] 14 years before Bloch published his eponymous equation [49]. The author recently derived from the Bloch equation, which Bloch

intended for macroscopic magnetization instead of individual nuclear magnetic moments [49], to the Schrödinger or Schrödinger–Pauli equation [17]. Kahraman *et al* demonstrated that the standard existing treatment of hyperfine interaction, consistent with the Breit–Rabi formula [38], cannot model the Frisch–Segrè experiment accurately but can be improved by incorporating CQD features [50]. The treatment also does not agree with the Rabi formula [16].

While no alternative theory, to the best of our knowledge, matches the Frisch–Segrè experiment, a recent multi-stage Stern–Gerlach experiment on superatomic icosahedral cage-clusters $Mn@Sn_{12}$ also reveals discrepancy of the Landau–Zener formula from experimental observation [51].

5. Conclusions

CQD, based on the sign-modified Landau–Lifshitz–Gilbert equation, provides a plausible collapse mechanism for electron spin in Stern–Gerlach experiments. CQD models both spin evolution and collapse by the same equations of motion. With an anisotropic angular distribution of co-quanta, CQD revises the wave function and accurately predicts the Frisch–Segrè experimental observation in absolute units without fitting with adjustable parameter, achieving $p < 8 \times 10^{-7}$—an objective statistical indication that reflects both correlation and degrees of freedom. Therefore, it is extremely unlikely that CQD happens to match the experimental observation so well by sheer chance. Further, with an isotropic angular distribution of co-quanta, CQD is theoretically corroborated by quantum mechanics. Both the strong experimental evidence and the exact quantitative agreement with quantum mechanics in diverse forms collectively support CQD. Like statistical mechanics [52], which uses molecular properties to predict macroscopic properties by ensemble averaging, CQD reproduces quantum mechanical properties by ensemble averaging over co-quanta (appendix 3). If orthodox quantum mechanics is incomplete [44], CQD may stimulate development for a complete theory.

Data availability statement

All data that support the findings of this study are included within the article (and any supplementary files).

Acknowledgments

The author thanks Dr Yixuan Tan for discussing the work, translating the German references using Google Translate, and drawing figure 3; Drs Zhe He and Kelvin Titimbo Chaparro for verifying the mathematical derivations and discussing the manuscript; Yixuan Tan, David Garrett, Kelvin Titimbo Chaparro, Siddik Suleyman Kahraman, and Zhe He for verifying CQD numerically (to be reported); Professor JT Shen and Mr. Siddik Suleyman Kahraman for discussing the manuscript; Professor Naisyin Wang and Mr. Sean Wang for discussing the statistics; Dr Victor Wang for discussing the math; and Professor James Ballard for editing an early version of the manuscript.

ORCID iD

Lihong V Wang https://orcid.org/0000-0001-9783-4383

References

[1] Gerlach W and Stern O 1922 Der experimentelle nachweis der richtungsquantelung im magnetfeld *Z. Phys.* **9** 349–52
[2] Schmidt-Böcking H, Schmidt L, Lüdde H J, Trageser W, Templeton A and Sauer T 2016 The Stern-Gerlach experiment revisited *Eur. Phys. J* **41** 327–64
[3] Castelvecchi D 2022 The Stern–Gerlach experiment at 100 *Nat. Rev. Phys.* **4** 140–2
[4] Einstein A and Ehrenfest P 1922 Quantentheoretische bemerkungen zum experiment von Stern und Gerlach *Z. Phys.* **11** 31–34
[5] Wennerström H and Westlund P-O 2012 The Stern–Gerlach experiment and the effects of spin relaxation *Phys. Chem. Chem. Phys.* **14** 1677–84
[6] Norsen T 2014 The pilot-wave perspective on spin *Am. J. Phys.* **82** 337–48
[7] Feynman R P, Leighton R B and Sands M L 1963 *The Feynman Lectures on Physics* (Reading, MA: Addison-Wesley Pub. Co)
[8] Phipps T E and Stern O 1932 Über die einstellung der richtungsquantelung *Z. Phys.* **73** 185–91
[9] Frisch R and Segrè E 1933 Über die einstellung der richtungsquantelung. II *Z. Phys.* **80** 610–6
[10] Majorana E 1932 Atomi orientati in campo magnetico variabile II *Nuovo Cimento* **9** 43–50
[11] Majorana E 2006 Oriented atoms in a variable magnetic field *Ettore Majorana: Scientific Papers* ed G Bassani (Berlin: Società Italian die Fisica and Springer) pp 125–32
[12] Landau L 1932 Zur theorie der energieubertragung. II *Phys. Z. Sowjetunion* **2** 46–51
[13] Zener C 1932 Non-adiabatic crossing of energy levels *Proc. R. Soc.* A **137** 696
[14] Stueckelberg E C G 1932 Theorie der unelastischen Stösse zwischen atomen *Helv. Phys. Acta* **5** 369
[15] Ivakhnenko O V, Shevchenko S N and Nori F 2023 Nonadiabatic Landau–Zener–Stückelberg–Majorana transitions, dynamics, and interference *Phys. Rep.* **995** 1–89
[16] Rabi I I 1936 On the process of space quantization *Phys. Rev.* **49** 324–8
[17] Wang L V 2022 Derivation from Bloch equation to von Neumann equation to Schrödinger–Pauli equation *Found. Phys.* **52** 61
[18] Carlesso M, Donadi S, Ferialdi L, Paternostro M, Ulbricht H and Bassi A 2022 Present status and future challenges of non-interferometric tests of collapse models *Nat. Phys.* **18** 243–50
[19] Ghirardi G C, Rimini A and Weber T 1986 Unified dynamics for microscopic and macroscopic systems *Phys. Rev.* D **34** 470–91
[20] Pearle P 1989 Combining stochastic dynamical state-vector reduction with spontaneous localization *Phys. Rev.* A **39** 2277
[21] Ghirardi G C, Pearle P and Rimini A 1990 Markov processes in Hilbert space and continuous spontaneous localization of systems of identical particles *Phys. Rev.* A **42** 78–89
[22] Steel R G D and Torrie J H 1960 *Principles and Procedures of Statistics* (New York: McGraw Hill)
[23] Rahman N 1968 *A Course in Theoretical Statistics* (New York: Charles Griffin and Company)

[24] Cousins R D 2017 The Jeffreys–Lindley paradox and discovery criteria in high energy physics *Synthese* **194** 395–432
[25] Abbott B P *et al* 2016 Observation of gravitational waves from a binary black hole merger *Phys. Rev. Lett.* **116** 6
[26] Grynberg G, Aspect A and Fabre C 2010 *Introduction to Quantum Optics: From the Semi-classical Approach to Quantized Light* (Cambridge: Cambridge University Press)
[27] Feynman R P, Vernon J F L and Hellwarth R W 1957 Geometrical representation of the Schrödinger equation for solving maser problems *J. Appl. Phys.* **28** 49–52
[28] Gilbert T L 2004 A phenomenological theory of damping in ferromagnetic materials *IEEE Trans. Magn.* **40** 3443–9
[29] Los Alamos National Laboratory: periodic table of elements (available at: https://periodic.lanl.gov/19.shtml)
[30] Norsen T 2017 *Foundations of Quantum Mechanics* (Berlin: Springer)
[31] Griffiths D J 2017 *Introduction to Electrodynamics* 4th edn (Cambridge: Cambridge University Press)
[32] Jackson J D 1999 *Classical Electrodynamics* 3rd edn (New York: Wiley)
[33] Ohanian H C 1986 What is spin? *Am. J. Phys.* **54** 500–5
[34] Rabi I I, Ramsey N F and Schwinger J 1954 Use of rotating coordinates in magnetic resonance problems *Rev. Mod. Phys.* **26** 167
[35] Forbes M D, Jarocha L E, Sim S and Tarasov V F 2013 Time-resolved electron paramagnetic resonance spectroscopy: history, technique, and application to supramolecular and macromolecular chemistry *Advances in Physical Organic Chemistry* ed I H Williams and N H Williams (Amsterdam: Elsevier) pp 1–83
[36] Marchione A A and Conklin B 2016 Gas phase NMR for the study of chemical reactions: kinetics and product identification *Gas Phase NMR* ed K Jackowski and M Jaszuński (Cambridge: Royal Society of Chemistry) pp 126–51
[37] Schroder W and Baum G 1983 A spin flipper for reversal of polarisation in a thermal atomic beam *J. Phys. E: Sci. Instrum.* **16** 52
[38] Breit G and Rabi I 1931 Measurement of nuclear spin *Phys. Rev.* **38** 2082
[39] Barra A L and Hassan A K 2005 Electron spin resonance *Encyclopedia of Condensed Matter Physics* ed F Bassani, G L Liedl and P Wyder (Oxford: Elsevier) pp 58–67
[40] Adler S L and Bassi A 2009 Is quantum theory exact? *Science* **325** 275–6
[41] Bricmont J 2016 *Making Sense of Quantum Mechanics* (Berlin: Springer)
[42] Laloë F 2019 *Do We Really Understand Quantum Mechanics?* (Cambridge: Cambridge University Press)
[43] Auletta G 2019 *The Quantum Mechanics Conundrum: Interpretation and Foundations* (Berlin: Springer)
[44] Einstein A, Podolsky B and Rosen N 1935 Can quantum-mechanical description of physical reality be considered complete *Phys. Rev.* **47** 777–80
[45] Frauchiger D and Renner R 2018 Quantum theory cannot consistently describe the use of itself *Nat. Commun.* **9** 3711
[46] Schrödinger E 1935 Die gegenwärtige situation in der quantenmechanik *Naturwissenschaften* **23** 807
[47] Titimbo K, Garrett D C, Kahraman S S, He Z and Wang L V 2022 Numerical modeling of the multi-stage Stern-Gerlach experiment by Frisch and Segre using co-quantum dynamics via the Bloch equation (arXiv:220813444)
[48] He Z, Titimbo K, Garrett D C, Kahraman S S and Wang L V 2022 Numerical modeling of the multi-stage Stern-Gerlach experiment by Frisch and Segre using co-quantum dynamics via the Schrodinger equation (arXiv:220814588)
[49] Bloch F 1946 Nuclear induction *Phys. Rev.* **70** 460–74
[50] Kahraman S S, Titimbo K, He Z, Shen J-T and Wang L V 2022 Quantum mechanical modeling of the multi-stage Stern-Gerlach experiment by Frisch and Segre using the von Neumann equation (arXiv:221011553)
[51] Fuchs T M and Schäfer R 2018 Double Stern-Gerlach experiments on $Mn@Sn_{12}$: refocusing of a paramagnetic superatom *Phys. Rev.* A **98** 063411
[52] Einstein A 1949 Remarks concerning the essays brought together in this co-operative volume *Albert Einstein: Philosopher-Scientist. Library of Living Philosophers* ed P A Schilpp (La Salle, IL: Open Court) pp 665–88
[53] Bjorken J D and Drell S D 1964 *Relativistic Quantum Mechanics* (New York: Mcgraw-Hill College)
[54] Gibbons J J and Bartlett J H 1935 The magnetic moment of the K^{39} nucleus *Phys. Rev.* **47** 692–4
[55] Hartree D R 1934 Results of calculations of atomic wave functions. II.—results for K^+ and Cs^+ *Proc. R. Soc.* A **143** 506–17
[56] Wittig C 2005 The Landau–Zener formula *J. Phys. Chem.* B **109** 8428–30